REPORT DOCUMENTATION PAGE

PLEASE DO NOT RETURN YOUR FORM TO THE ABOVE ORGANIZATION.

1. REPORT DATE *(DD-MM-YYYY)*	2. REPORT TYPE	3. DATES COVERED *(From - To)*
16-03-2009	Final Report	02/15/06 to 11/30/08

4. TITLE AND SUBTITLE
SUPER MANEUVERABLE, FLAPPING WING MICRO-AIR VEHICLES

5a. CONTRACT NUMBER

5b. GRANT NUMBER
FA9550-06-1-0093

5c. PROGRAM ELEMENT NUMBER

6. AUTHOR(S)
B. Balachandran and E. Balaras

5d. PROJECT NUMBER

5e. TASK NUMBER

5f. WORK UNIT NUMBER

7. PERFORMING ORGANIZATION NAME(S) AND ADDRESS(ES)
Department of Mechanical Engineering
University of Maryland
College Park, MD 20742-3035

8. PERFORMING ORGANIZATION REPORT NUMBER

9. SPONSORING/MONITORING AGENCY NAME(S) AND ADDRESS(ES)
Dr. Victor Giurgitiu
Program Manager, Structural Mechanics
AFOSR/NA
875 North Randolph St, Suite 325, Room 3112, Arlington, VA 22203-1768

10. SPONSOR/MONITOR'S ACRONYM(S)

11. SPONSOR/MONITOR'S REPORT NUMBER(S)

12. DISTRIBUTION/AVAILABILITY STATEMENT
DISTRIBUTION A; APPROVED FOR PUBLIC RELEASE

13. SUPPLEMENTARY NOTES

14. ABSTRACT
Interest in the development of super-maneuverable, micro-air-vehicles has led to the re-examination of basic flight modes, particularly, those that are inspired by biological observations. The majority of experimental and numerical studies related to flapping flight have explored the relationships between the thrust coefficient (and propulsive efficiency) and wing geometry and kinematics. Relatively speaking, the wing flexibility and the interplay between kinematics and flexibility have received less attention, and currently, it remains unclear as to if they can be exploited to achieve a better performance during low Reynolds number flapping flight. To bridge this gap, the role of flexibility and fluid-structure interactions in flapping flight have been numerically investigated by using a two-dimensional, two-component wing system with a torsion spring. One of the primary outcomes of this work is that nonlinear resonances play an important role in determining the performance of a flapping wing system, mainly through the formation of leading, trailing edge, and end of stroke vortices and interactions amongst them.

15. SUBJECT TERMS
flapping wing, fluid-structure interactions, wing flexibility, nonlinear resonances, low Reynolds numbers, high fidelity schemes, low fidelity schemes

16. SECURITY CLASSIFICATION OF:			17. LIMITATION OF ABSTRACT	18. NUMBER OF PAGES	19a. NAME OF RESPONSIBLE PERSON
a. REPORT	b. ABSTRACT	c. THIS PAGE			B. Balachandran
					19b. TELEPHONE NUMBER *(Include area code)* (301)405-5309

SUPER MANEUVERABLE, FLAPPING WING MICRO-AIR-VEHICLES

AFOSR GRANT [redacted] FA9550-06-0093

B. Balachandran and E. Balaras
Department of Mechanical Engineering
University of Maryland
College Park, MD 20742-3035

Abstract

Interest in the development of super-maneuverable, micro-air-vehicles has led to the re-examination of basic flight modes, particularly, those that are inspired by biological observations. The majority of experimental and numerical studies related to flapping flight have explored the relationships between the thrust coefficient (and propulsive efficiency) and wing geometry and kinematics. Relatively speaking, the wing flexibility and the interplay between kinematics and flexibility have received less attention, and currently, it remains unclear as to if they can be exploited to achieve a better performance during low Reynolds number flapping flight. To bridge this gap, the role of flexibility and fluid-structure interactions in flapping flight have been numerically investigated by using a two-dimensional, two-component wing system with a torsion spring. One of the primary outcomes of this work is that nonlinear resonances play an important role in determining the performance of a flapping wing system, mainly through the formation of leading, trailing edge, and end of stroke vortices and interactions amongst them.

Key words: flapping wing, fluid-structure interactions, wing flexibility, nonlinear resonance, low Reynolds numbers

Manuscript Summarizing Results on the Influence of Flexibility Follows

Influence of flexibility on the aerodynamic performance of a hovering wing

Marcos Vanella, Timothy Fitzgerald, Sergio Preidikman, Elias Balaras, and Balakumar Balachandran*

Department of Mechanical Engineering, University of Maryland
College Park, MD 20742, USA
*Author for correspondence (e-mail: balab@umd.edu)

Summary

In the present work, a computational investigation is carried out to understand the influence of flexibility on the aerodynamic performance of a hovering wing. A flexible, two-dimensional, two-link model moving within a viscous fluid is considered. The Navier-Stokes equations governing the fluid dynamics are solved together with the equations governing the structural dynamics by using a strongly coupled fluid-structure interaction scheme. Harmonic kinematics is used to prescribe the motions of one of the links, thus effectively reducing the wing to a single degree-of-freedom oscillator. The wing's flexibility is characterized by the ratio of the flapping frequency to the natural frequency of the structure. Apart from the rigid case, different values of this frequency ratio (only in the range of 1/2 to 1/6) are considered at the Reynolds numbers of 75, 250, and 1000. It is found that flexibility can enhance the aerodynamic performance and that the best performance is realized when the wing is excited by a nonlinear resonance at one-third of the natural frequency. Specifically, at the Reynolds numbers of 75, 250 and 1000, the aerodynamic performance that is characterized by the ratio of lift coefficient to drag coefficient is respectively increased by 28%, 23%, and 21% when compared with the corresponding ratios of a rigid wing driven with the same kinematics. For all Reynolds numbers, the lift generated per unit driving power is also enhanced in a similar manner. The wake capture mechanism is enhanced, due to a stronger flow around the wing at stroke reversal, resulting from a stronger end of stroke vortex at the trailing edge. The present study provides some clues about how flexibility affects the aerodynamic performance in low Reynolds number flapping flight. In addition, it points to the importance of considering nonlinear resonances for enhancing aerodynamic performance.

Key words: flapping wing, fluid-structure interactions, finite-difference method, wing flexibility, nonlinear resonance, low Reynolds numbers

Introduction

Over the past decade, insect flight has attracted a lot of interest in a variety of disciplines in science and engineering. As a result, many experimental investigations (e.g., Ellington, Van den Berg, Wilmott, and Thomas, 1996; Dickinson, Lehmann, and Sane, 1999) as well as computational investigations (e.g., Liu and Kawachi, 1998; Sun and Tang, 2002; Ramamurti and Sandberg, 2002, 2006; Wang, 2000a, 2000b; Wang, Birch, and Dickinson, 2004) have been reported in the literature. The aim of most of these studies has been the understanding of complex, unsteady mechanisms that enable the generation of aerodynamic forces for hovering and maneuvering. Insect wings are complex structures that during flapping undergo deformations due to aerodynamic forces, elastic forces, as well as inertia forces due to the accelerations experienced by the system mass. The wing structural behavior depends, to a large extent, on the internal distribution of compliant components and mechanisms (Wootton, 1999). It is important to note that insect wings lack internal muscles, and hence, there are no actuators to realize internal control forces (Wootton, Herbert, Young, and Evans, 2003).

In a variety of species, the roles of inertial, elastic, and aerodynamic forces during flapping flight have been the focus of many investigations (see for example, Ellington, 1984b; Ennos, 1989; Lehman and Dickinson, 1997; Sun and Tang, 2002; Daniel and Combes, 2002; Combes and Daniel, 2003; Song, Wang, Zeng, and Yin, 2001). It is difficult to make direct comparisons between the different studies, not only because the studies usually involve different species, but also because different approaches have been used to compute the forces. For example, Combes and Daniel (2003) assessed the relative contributions of aerodynamic, inertial, and elastic forces to the wing deformation of the *Manduca sexta* hawkmoth. They concluded that the wing motion of this particular insect is mostly determined by the wing inertia and elastic forces with the aerodynamic loads providing damping. During hovering, they found that the typical ratio of wing inertia force to aerodynamic force is about seven. This result was obtained by using scaling arguments and assuming a weight balance to get a fluid-force estimate. In other species, this ratio has been found to be much lower. Ennos (1989), for example, showed that for several species of *Diptera*, the magnitudes of inertia bending moments are about twice that of the magnitudes of aerodynamic moments during harmonic flapping. Also, in this case, the analysis was based on the weight-balance assumption and harmonic kinematics. However, unlike Combes and Daniel (2003), they considered the effect of the virtual or added mass of the surrounding fluid. It should be noted that in the studies of Ennos (1989) and Combes and Daniel (2003), the aerodynamic forces are underestimated, since the drag component of the fluid force is neglected.

With increase in computational power, computational models of insect flight have become sophisticated. Two-dimensional computations (e.g., Wang, 2000a, 2000b; Miller and Peskin 2005, Miao and Ho 2006) and three-dimensional computations (e.g., Liu and Kawachi, 1998; Ramamurti and Sandberg, 2002, 2006; Sun and Tang, 2002) with various

degrees of complexity have been reported. In general, for low ratios of inertia to aerodynamic forces, one can expect complex aeroelastic interactions to occur. An interesting open question within this context is the following: *How does structural flexibility affect the aerodynamic performance of a given flapping wing* and w*hat is the effect of the Reynolds number?* The present study attempts to address this question by using computational investigations. To the best of the authors' knowledge, no prior computational studies addressing this question have been carried out.

In the present study, in order to explore a fairly wide parametric regime in a cost-efficient manner, the authors limit themselves to studies in two dimensions. A representative section of the wing (two-dimensional foil) is used in this study, and spanwise bending and torsion flexibility are discarded. A two-link structure connected with a torsion spring is used to account for deformation in the chordwise direction. This system has four degrees of freedom, which are effectively reduced to one, by prescribing harmonic hovering motions of one of the links. The links are considered to be rigid in the present work, and they are currently being extended to flexible beams in ongoing efforts. The large angular deformations of the links give rise to cubic and higher order odd nonlinearities in the governing equations like those seen in equations governing a pendulum as well as flexible beams (e.g., Anderson, Balachandran, and Nayfeh, 1994). In a sense, one could consider the two links as a double pendulum with a torsion spring. Fluid nonlinearities are also considered here. Different values of the torsion spring stiffness are considered at the Reynolds numbers of 75, 250, and 1000, and the results obtained are reported in the form of mean lift force, mean drag force, ratio of lift to drag, and ratio of mean lift coefficient to total power input. The performance of the hovering wing is also examined when it is excited at a nonlinear resonance of the structural system.

In the following section, a description of the system is provided along with the computational formulation. Then, the parametric space and system kinematics are detailed. Next, results and discussion sections follow, with a closure section at the end.

System description and computational formulation

As aforementioned, the authors consider a section of a three-dimensional wing and accounts for chordwise deformations, but do not account for spanwise bending and torsion flexibility. As shown in Figure 1, the considered structural system consists of two rigid links A and B, which are joined at the center b by a pin that contains a linear torsion spring. In the current model, flexibility is concentrated at one discrete location of the structural system, and inclusion of elastic links will allow one to account for chordwise variations of stiffness and mass. For computational purposes, the two links are covered by a set of aerodynamic surfaces that define the boundary between the airfoil and the fluid, and deform as the angle between the two links changes. The aerodynamic surfaces consist of two rigid segments, R_{Sa} and R_{Sb} (see Figure 1B), and two segments that dynamically deform according to the angle between the two links. The deformation is prescribed by fitting the Hermite interpolation polynomials c_1-c_2 and c_3-c_4. The authors

have found that this modeling is robust and helps maintain the smoothness of the surface even for large values of the angle between the plates (large deformation configurations).

System equations

The flapping motions of the chosen two-dimensional configuration in a fluid are governed by a coupled system of equations descriptive of the respective fluid and structural mechanics. The fluid dynamics is governed by the Navier-Stokes equations for an incompressible flow; that is,

$$\frac{\partial u_i}{\partial t}+\frac{\partial}{\partial x_j}\left(u_i u_j\right)=-\frac{\partial p}{\partial x_i}+\frac{1}{\mathrm{Re}}\frac{\partial^2 u_i}{\partial x_j \partial x_j}+f_i, \tag{1}$$

$$\frac{\partial u_i}{\partial x_i}=0\ , \tag{2}$$

where t is the time, x_i (i=1,2) is the spatial coordinate in the i^{th} Cartesian direction, u_i is the corresponding velocity, p is the pressure, and f_i is an external body force. The above equations have been made dimensionless by using the chord length of the undeformed plate, L_c, as the reference length scale, and the maximum translational velocity at the junction of the links, U_c, as the reference velocity scale. The Reynolds number is defined as $\mathrm{Re}=\rho_f L_c U_c/\mu$, where ρ_f and μ are the fluid density and viscosity, respectively.

The dimensionless form of the equations governing the motion of the structural system shown in Figure 1 can be derived as

$$\begin{bmatrix} m_A+m_B & 0 & \begin{pmatrix}-m_A\eta_A\sin(\alpha+\theta)\\ +m_B\eta_B\sin(\theta)\end{pmatrix} & -m_A\eta_A\sin(\alpha+\theta) \\ & m_A+m_B & \begin{pmatrix}-m_A\eta_A\cos(\alpha+\theta)\\ +m_B\eta_B\cos(\theta)\end{pmatrix} & m_A\eta_A\cos(\alpha+\theta) \\ & & I_A+I_B & I_A \\ \textit{symmetric} & & & I_A \end{bmatrix} \begin{Bmatrix}\ddot{x}\\ \ddot{y}\\ \ddot{\theta}\\ \ddot{\alpha}\end{Bmatrix} = \begin{Bmatrix}Q_x+g_x\\ Q_y+g_y\\ Q_\theta+g_\theta\\ Q_\alpha+g_\alpha\end{Bmatrix}, \tag{3}$$

where $x(t)$, $y(t)$, and $\theta(t)$ are respectively the joint horizontal motion, joint vertical motion, and orientation angle of link B measured from an inertial reference frame as shown in Figure 1A, and $\alpha(t)$ is the deflection angle between links A and B. Here, m_i is the total mass of the ith link (i=A, B), η_i is the distance from the junction to the center of mass of bar i as shown in Figure 1A, and I_i is the moment of inertia of link i with respect to the hinge point b. Also, Q_x and Q_y are the fluid forces along the x and y directions, respectively, and Q_θ and Q_α are the fluid moments associated with the generalized

coordinates $\theta(t)$ and $\alpha(t)$, respectively. The quantities $g_x, g_y, g_\theta,$ and g_α are the corresponding contributions of centrifugal, elastic, and gravity forces. The reference length scale and velocity defined above, together with the fluid density are used to make system (3) dimensionless. The fluid forces and moments are determined from equations (1) and (2).

In the numerical experiments conducted in this study, the translational motions of the junction, as well as the orientation of link *B* are prescribed. With these prescribed motions, the four degrees of freedom of the system can be effectively reduced to one; that is, the deflection angle $\alpha(t)$ between plates *A* and *B*. Thus, the overall deformation of the wing section is determined by the deflection angle $\alpha(t)$, which is governed by the following reduced form of system (3):

$$I_A\ddot{\alpha} + k\alpha = -I_A\ddot{\theta} + m_A\eta_A \sin(\theta+\alpha)\ddot{x} + Q_\alpha . \tag{4}$$

Equation (4) resembles the equation governing a harmonic oscillator with forcing due to the prescribed kinematics and the fluid forces (e.g., Nayfeh and Balachandran, 1995). The nonlinearities arise from the $\sin(\theta+\alpha)$ term due to the kinematics and the fluid forcing. For this particular study, the authors only take into account the fluid damping which arises through the fluid moment Q_α . It should be noted that selecting a proper structural damping model is far from trivial, and this is an active research topic in structural biomechanics. Damping models for insect wings are relatively few (e.g., classical viscous damping model used by Herbert, 2002 and the viscoelastic model used by Bao, Hu, Yu, Cheng, Xu, and Tong, 2006) and the existing models require a fair amount of empirical information.

Prescribed kinematics, parameter values, and computational formulation

To prescribe the translational motions of the junction and the orientation of link *B*, the authors define the states *x(t)*, *y(t)*, and *θ(t)* as

$$x(t) = \left(1 - e^{-\frac{t}{\tau}}\right)\frac{A_o}{2}\cos(\omega_f t) \quad ; \quad y(t) = 0 \quad ; \quad \theta(t) = \theta_o + \left(1 - e^{-\frac{t}{\tau}}\right)\gamma\sin(\omega_f t + \phi) , \tag{5}$$

where A_o is the stroke length of the pin point, θ_o is the mean orientation angle for link *B*, γ is the rotation amplitude, ω_f is the frequency of the prescribing or forcing oscillation and ϕ is the phase angle between $x(t)$ and $\theta(t)$. The exponential terms are used in order to reduce transient effects (Combes and Daniel, 2003). The time constant is chosen as $\tau = 1.6 * \pi / \omega_f$, since 99.8% of the prescribed amplitude is reached after a time length of 5 periods. The following parameters corresponding to symmetric hovering are selected (Wang *et al.*, 2004):

$$A_o = 2.8 \quad ; \quad \theta_o = -\frac{\pi}{2} \quad ; \quad \gamma = \frac{\pi}{4} \quad ; \quad \phi = 0 \tag{6}$$

Based on the adopted normalization, the problem is completely defined by the density ratio ρ_b / ρ_f, frequency ratio ω_f / ω_n, and the Reynolds Number Re. Here, ρ_b is the density of the wing's material, and $\omega_n = \sqrt{k / I_A}$ is the linear natural frequency of the oscillator (4). The frequency ratio ω_f / ω_n is used to characterize the flexibility of the wing section.

Three Reynolds numbers are considered (Re=75, 250 and 1000) to investigate the effect of the reduction in viscous dissipation on the system dynamics. The mass ratio is set to $\rho_A / \rho_f = 25$, since this value provided a ratio close to 2 for the maximum translational inertia force over maximum drag force at Re =75, for the chosen geometry and kinematics. The above ratio was determined through numerical experiments with the rigid wing. To compute the maximum horizontal translational inertia force, the total wing mass is multiplied by the maximum acceleration determined from the second derivative of *x(t)* in equation (5). The value of peak drag force, on the other hand, is obtained from the rigid wing simulation at Re=75. The wing has a thickness of 10% of the undeformed chord length and circularly formed edges. For the simulations conducted at Re=75, the frequency ratio ω_f / ω_n is set to 1/2, 1/2.5, 1/3, 1/3.5, 1/4, and 1/6. For Re = 250 and 1000, this ratio is set to 1/2, 1/3, 1/4, and 1/6. The resulting range of maximum deflection angles varied from 10° to 70°. Also, the rigid wing problem (no angular deformation between the links) was run for all of these Reynolds numbers. It should be noted that for frequency ratios below 1/2, the computations would fail since the two plates collide during rotation. This limitation arises from the fact that the flexibility in the present model is concentrated at the hinge point and the distributed chordwise variations of stiffness and mass is not accounted for. A flexible beam model and/or inclusion of structural damping may help to address this issue and enable computations with frequency ratios of about one.

Equations (1), (2), and (4) governing the dynamics of the fluid-structure system are numerically solved by using a strongly coupled, embedded-boundary formulation. The overall approach is a mixed Lagrangian-Eulerian formulation, where equations (1)-(2) governing the fluid flow are solved on a fixed Cartesian grid, which is not aligned with the wing surface, and the non-slip conditions are enforced via local reconstructions of the solution near the solid interface (see, for example Balaras, 2004, Uhlmann, 2005, Yang and Balaras, 2006). The fluid and the structure are treated as elements of a single dynamical system, and all governing equations are integrated simultaneously and interactively in the time-domain by using a predictor-corrector scheme. Further details on the coupling scheme and the overall fluid-structure interaction algorithm can be found in the work of Yang, Preidikman, and Balaras (2008).

Results

In this section, computations of aerodynamic forces are presented for three different Reynolds numbers and different wing flexibility values. Comparisons are also made between the results obtained for the rigid wing and flexible wing cases and with the results obtained by Wang *et al.* (2004).

Computational setup

The computational grid was carefully selected to resolve the thin boundary layers and detached shear layers on the moving links and the wake vortical structures for the different Reynolds numbers considered in this study. The rigid wing was set to move in the center of a box with the dimensions of 30 $L_c \times 30\ L_c$, in order to minimize interference effects from the far-field boundaries. A near uniform grid zone was generated near the center, where the motions of the two-link system took place, and this zone was stretched towards the boundaries. For the Re = 75 simulations, the uniform grid zone had a local cell size of $\Delta x = \Delta y = 0.0038 L_c$, and the total number of points was 1229 x 551 along the x and y directions, respectively. Through grid refinement studies, the authors found that the above resolution was sufficient to capture all flow features. In Figure 2, computationally obtained aerodynamic forces are shown for approximately half the resolution throughout the computational domain (total number of points was 664x400) and the same forcing conditions (i.e., $\tau = 0$ in equations (5)) and Reynolds number as that for the baseline rigid wing computation. The corresponding lift and drag coefficients determined in the computations of Wang *et al.* (2004), where a hovering ellipse with the same kinematics is considered instead of a plate, is also included in the figure. The agreement between the results obtained with the two different grids is good with a maximum difference of around 3%. Despite the differences in the wing-section shapes, after the initial transients ($t/T>2$), good agreement is also seen with the results obtained by Wang *et al.* (2004).

For the results of Figure 2, within the boundary layers on the link surface, the authors estimated the number of grid points to be approximately 8 and 16 for the coarse and fine grids, respectively. As the Reynolds number increases, the boundary layer thickness is expected to decrease as $1/\sqrt{\mathrm{Re}}$, and in order to keep the resolution within the above range, a grid with 1320 × 1038 points was found to be sufficient for both Re = 250 and 1000 cases. All the results presented in this article have been obtained with a 1229 × 551 grid for the Re = 75 simulations and a 1320 × 1038 grid for the Re = 250 and Re = 1000 simulations. The governing equations were integrated for a time length of 14 periods, 21 periods, and 15 periods, for Re = 75, 250, and 1000, respectively. The time-averaged quantities were computed over the last 7 periods, 13 periods, and 10 periods, for Re = 75, 250, and 1000, respectively.

Aerodynamic quantities

For the flexible wings considered in this study, the lift and drag coefficients are defined as

$$C_L(t) = \frac{Q_y^*(t)/L_c}{\frac{1}{2}\rho_f \cdot U_c^2 L_c} = 2Q_y(t) \;;\; C_D(t) = -\frac{sgn(\dot{x}(t))\; Q_x^*(t)/L_c}{\frac{1}{2}\rho_f \cdot U_c^2 L_c} = -2sgn(\dot{x}(t))Q_x(t), \quad (7)$$

where the quantities $Q_x^*(t)$ and $Q_y^*(t)$ are dimensional quantities and $Q_x(t)$ and $Q_y(t)$ are non-dimensional quantities. Once the equation for the deformation $\alpha(t)$ is solved at each iteration, the driving forces in the prescribed generalized coordinates $x(t)$, $y(t)$, and $\theta(t)$ are computed from the system (3). The total power input, which is the sum of horizontal translation power and rotation power, can be computed from

$$\begin{aligned} P_{tr} &= R_x(t) \cdot \dot{x}(t) \\ P_{rot} &= R_\theta(t) \cdot \dot{\theta}(t) \end{aligned} \quad (8)$$

where P_{tr} and P_{rot} are the translational and rotational power inputs at the hinge b, $R_x(t)$ is the driving force in the x direction, and $R_\theta(t)$ is the driving moment in the $\theta(t)$ angular direction. In an ideal case were the driving mechanism is perfectly elastic and the negative power provided to the mechanism can be stored as potential energy for later use, this power will enhance the wing's aerodynamic efficiency. Here, following Berman and Wang (2007), a conservative approach is used and it is assumed that the negative power is not available for reuse; that is,

$$P_{tr} = \begin{cases} P_{tr}, & if\ P_{tr} > 0 \\ 0, & if\ P_{tr} < 0 \end{cases}, \quad P_{rot} = \begin{cases} P_{rot}, & if\ P_{rot} > 0 \\ 0, & if\ P_{rot} < 0 \end{cases} \quad (9)$$

The power coefficient is defined as

$$C_{PW}(t) = \frac{(P_{tr}^*(t) + P_{rot}^*(t))/L_c}{\frac{1}{2} \cdot \rho_f \cdot U_c^3 \cdot L_c} = 2(P_{tr}(t) + P_{rot}(t)), \quad (10)$$

where $P_{tr}^*(t)$ and $P_{rot}^*(t)$ are dimensional quantities and $P_{tr}(t)$ and $P_{rot}(t)$ are non-dimensional quanitites.

In Figure 3, the variations of the mean values of C_L and C_D and the aerodynamic performance ratios C_L/C_D and C_L/C_{PW} with respect to the frequency parameter ω_f / ω_n are shown. The rigid wing has zero torsion stiffness or equivalently $\omega_n = 0$. For all cases, the lift and drag coefficients exhibit a peak at a frequency ratio $\omega_f / \omega_n = 1/3$. The performance ratio C_L/C_D also exhibits a prominent peak at this frequency ratio. For Re = 75, 250, and 1000, increases of about 28%, 23%, and 21% over those obtained for the

rigid wing are observed, respectively. The variations of the aerodynamic quantities with respect to the frequency ratio show similar characteristics for all three Reynolds numbers. However, it is interesting to note the striking difference between the graph of C_L/C_D obtained for the Re = 75 case and those obtained for the higher Reynolds numbers. For the lowest Reynolds number and $\omega_f/\omega_n = 1/4$, the above ratio is over 13% higher than that obtained for the rigid wing, while for Re=250, it is increased only by 0.5%. In Figure 3C, it is seen that for $\omega_f/\omega_n = 1/3$, the performance ratio C_L/C_{PW} is 39% and 28% higher than the obtained for the rigid wing for Re = 75 and Re = 250 cases, respectively. Interestingly, this measure is only about 13% higher than that obtained for the rigid case at Re = 1000.

In Figure 4, the time histories of the lift and drag coefficients are shown for all Reynolds numbers at three selected frequency ratios. The effects of flexibility are noticeable on the lift-force peaks at the initiation of stroke (indicated with a black arrow in the figure). For Re=75 and $\omega_f/\omega_n = 1/2$, corresponding to the most flexible foil, this peak is negative, while for the rigid case the coefficient of lift peaks at 0.5. For all cases in between, the enhancement on the mean lift force seen in Figure 3 comes from the gradual increase of this peak, which is at 0.83 and 1.28 for $\omega_f/\omega_n = 1/4$ and $\omega_f/\omega_n = 1/3$, respectively. For the latter frequency ratio, where a structural nonlinear resonance occurs, the lift peak is also delayed and nearly coincides with the translational lift peak. This is translated into a larger area under the lift curve per period and a larger time averaged C_L value. The temporal variations of lift and drag coefficients for Re = 250 and 1000 is more complex than the variations seen at Re = 75, and the periodicity is practically lost. Still, in an average sense, negative lift peaks after stroke reversal and larger translational lift peaks are seen when $\omega_f/\omega_n = 1/2$. Also, a widened two-peak lift curve is observed when $\omega_f/\omega_n = 1/3$.

Vortex structures

In order to relate the temporal variations of the lift and drag forces to specific flow structures, the authors carefully examined several realizations of the instantaneous flow fields. In Figure 5, vorticity isolines are shown for the rigid and $\omega_f/\omega_n = 1/3$ cases at Re =7 5. For clarity, the lift coefficient variation has been added (Figure 5K), together with the temporal variation of the phase-averaged circulation of the most important vortical structures generated during a flapping cycle. These are the leading edge vortex (LEV) shown in Figure 5A, the end of stroke vortex (ESV) shown in Figure 5C, and trailing edge vortex (TEV) shown in Figure 5E. The circulation of each of these vortices has been computed as a function of time by direct integration of the vorticity within a given threshold contour around each vortex. The selection of the threshold contour, although arbitrary, has been consistently taken to be the lowest closed vorticity isoline in the vicinity of the given vortex.

As the flexible wing approaches the end of stroke in Figure 5A, it exhibits different rotation velocities on the two components *A* and *B*. The driven link *B* rotates with the

prescribed angular velocity $\dot{\theta}(t)$, and the lower link *A*, rotates with an angular speed $\left(\dot{\theta}(t)+\dot{\alpha}(t)\right)$. The effect of the added angular speed $\dot{\alpha}(t)$ affects the overall dynamics at stroke reversal. First, the camber generated by the angular deformation $\alpha(t)$ at the end of stroke (see Figure 5B) reorients the zero lift direction on the wing and enhances wake capture effects. This enhancement mechanism is analogous to the one produced by orientation advancement in rigid wings (e.g., Wang *et al.* 2004). It is important to note that an excessive degree of flexibility (low frequency ratios) produces a large camber at stroke reversal, which has a negative effect on the lift production (e.g., at $\omega_f / \omega_n = 1/2$ in Figure 4). The evolution and strength of the LEV on the other hand (see Figure 5A) is only a weak function of the wing's flexibility. The formation time as well as the maximum circulation shown in Figure 5L are approximately the same for both the rigid and the flexible wings.

Another effect of the higher rotation speeds at the trailing edge for the flexible wings is the formation of a stronger shear layer, which rolls-up into a stronger ESV (see Figure 5C). On examining the ESV circulation plots (Figure 5K), one finds that the strength and life span is significantly enhanced when compared with those of a rigid wing. The ESV pinches-off later, forming a pair of counter rotating vortices together with the LEV. This vortex pair generates flow directed towards the wing enhancing the wake capturing effects. This is more clearly reflected in the lift coefficient evolution shown in Figure 5K. In contrast to the rigid wing, where the lift curve reaches a maximum (point H) and starts to decrease, for the flexible wing the production of increased lift continues longer (point C).

Once a flexible wing's deflection has reached its maximum, the elastic energy stored in the torsion spring is released to generate a restoring motion, whose timing again depends on the degree of flexibility of the structure (see Figures 5D and 5E). This restoring motion produces a dynamical change of the wing's camber with a resulting increase in the fluid forces. This also affects the formation and growth of the TEV. It is well established that this flow structure generates a low-pressure zone, which translates into increasing forces up to the pinch-off time (see for example Wang, 2000b). The time at which the TEV pinches off is correlated with the translational force peak; this peak happens much later in the $\omega_f / \omega_n = 1/3$ case when compared with that for the rigid wing.

In Figure 6, a quantitative comparison of the LEV, ESV, and TEV dynamics is made for different flexibilities at Re = 75 by determining their average circulations as a function of time. The maximum averaged circulation for each vortex and the time at which it occurs with respect to the stroke reversal are provided in Table 1. As expected, from what was observed in Figure 5, the LEV dynamics is similar for all frequency ratios both in terms of strength and timing. The TEV on the other hand, attains a higher maximum circulation as the wing becomes more flexible. However, the time it takes to reach this maximum circulation is shortest for $\omega_f / \omega_n = 1/3$, where the best aerodynamic performance is seen. For the ESV vortex, the maximum circulation increases for the frequency ratios $\omega_f / \omega_n = 1/3$ and $1/4$. The peak circulation for $\omega_f / \omega_n = 1/3$ is 20% lower than that

obtained for $\omega_f / \omega_n = 1/4$, but the deflection at stroke reversal in terms of the maximum deformation angle is 90% larger when $\omega_f / \omega_n = 1/3$ (56 degrees for $\omega_f / \omega_n = 1/3$ and 29 degrees for $\omega_f / \omega_n = 1/4$). This is translated into a larger projected area contributing to the lift force. Also, as seen from Figure 6, the time delay of the peak circulation of the ESV vortex is increased as the wing becomes more flexible.

A more direct illustration of the abovementioned vortex evolutions is given in Figure 7, where instantaneous vorticity isolines are shown for eight characteristic instances during a flapping cycle. For $\omega_f / \omega_n = 1/3$ and $1/4$, it is clear that the enhanced ESV vortices produce an oblique shaped TEV vortex. For $\omega_f / \omega_n = 1/2$, an excessive negative camber is produced at stroke reversal, which then generates a high suction zone on the lower side of the wing leading to the negative peak in the C_L curve seen in Figure 4. The Reynolds number effects on the temporal evolution of the lift and drag forces seen in Figure 4 can also be observed in Figure 8, where the instantaneous vorticity isolines are shown for Re = 250 for all frequency ratios. Clearly, as the viscous damping is decreased, the system dynamics system ceases to be periodic and the important vortices are stronger and are not dissipated as quickly as seen in the Re = 75 case (see Figure 7). For the case of a rigid wing, for example, the LEV from a given stroke interacts with the shear layer being generated in the next stroke, and this induces a premature formation of the new LEV. This process is not periodic, which is also reflected in the evolution of lift and drag forces. A similar interaction is observed at $\omega_f / \omega_n = 1/2$ (see last three frames in Figure 8B).

Discussion

Insect wings are flexible structures that undergo large displacements and deformations during flapping, as the wing structures interact with the surrounding flow. There has been speculation that many insects flap their wings at frequencies close to the natural frequency of the structure. For example, analysis of the *Manduca sexta* wings (see Combes and Daniel, 2003 and Wootton, 2003) has shown that the wing's first natural frequency is close to the driving frequency in normal flapping motion. This suggests that insects may be taking advantage of a structural resonance to reduce energy consumption and enhance aerodynamic performance. Despite the significance of such a hypothesis, only a limited number of studies have addressed the problem due to the exceedingly complex fluid-structure interactions that are encountered in experimental or numerical work. Although three-dimensional computations of the Navier-Stokes system coupled with a wing structural system are within the reach of today's computers, one still needs to develop appropriate mathematical models and tools to capture all important phenomena in this complex system. In this regard, the present study extends computational work that has been conducted before with simplified two-dimensional rigid wings to include the effects of flexibility. The wing is represented by two rigid links, which are joined at the center by a pin that contains a torsion spring. The kinematics of one of the links is prescribed, while the motion of the other link is determined by the fluid-structure interactions. Although, a fairly wide range of Reynolds numbers and frequency ratios has been examined, the authors found that the computations would fail for forcing

frequencies close to the linear resonance frequency due to an excessive degree of flexibility. This limitation is due to the concentration of flexibility at a discrete point, and the replacement of rigid links with elastic links modeled as elastic beams is expected to help in overcoming this limitation.

As mentioned earlier, the two link structural system can be perceived as a double pendulum with a common hinge. In particular, when one of the link motions is prescribed, the other link behaves as a pendulum subjected to a constraint arising from the prescribed motion and complex fluid-structure interactions. Equation (4) does resemble the equation of a pendulum driven in a fluid. A straightforward perturbation analysis (e.g., Nayfeh and Balachandran, 1995) shows that the structural system can exhibit nonlinear resonances at $\omega_f = 1/3\,\omega_n$ and $\omega_f = 3\,\omega_n$. These resonances are expected in systems with cubic nonlinearities, for example, in the equations governing local oscillations of a pendulum about an equilibrium position and elastic systems such as beams (e.g., Anderson *et al*., 1994). Operation of the flexible wing at the nonlinear superharmonic resonance $\omega_f = 1/3\,\omega_n$ is seen to beneficial for the aerodynamic performance. Inclusion of fluid effects will give rise to quadratic nonlinearities and additional nonlinear resonances.

For the specific set of kinematics that the authors considered, most of the benefits of having a flexible wing are associated with the stroke reversal phase of the cycle. Especially for the optimal flexibility cases ($\omega_f = 1/3\omega_n$), the strength and timing of the ESV, as well as the dynamical changes of the wing's camber due to structural deformations, are responsible for the performance enhancement. The overall enhancement mechanism is analogous to the one produced by orientation advancement in rigid wings (see for example, Wang *et al.* 2004). It is noted that the present computations cover a wide range of frequency ratios, and consequently, wing deflections range from a few degrees to very large values. For example, in the case of highly stiff wings (e.g., $\omega_f / \omega_n = 1/6$), maximum deflection angles between the links was about 11°, 13° and 16° for Re = 75, 250, and 1000 respectively, while for highly flexible wings (e.g., $\omega_f / \omega_n = 1/2$), the corresponding numbers were 67°, 68°, and 91°, respectively. In insects, the wing deformation magnitudes increase as the body size and mass increase, and it is conceivable that deformations seen in this study at the aerodynamically preferred frequency ratio of $\omega_f / \omega_n = 1/3$could be possible in some species. On the other hand, for small insects such as the *Drosophila*, only small magnitude wing deformations have been observed. The computations of this study show that as the wing is made stiffer, the performance enhancements are marginal when compared to a rigid foil. For example, at Re = 75 and the highly stiff case $\omega_f / \omega_n = 1/6$, the C_L/C_D is approximately 6% higher when compared to that of a rigid foil. For the higher Reynolds numbers Re = 250 and 1000, there is actually no enhancement, and the performance is worse than that obtained with a rigid foil. The above results indicate that low Reynolds number regimes might benefit in performance even at small chordwise distortions.

The force histories, in particular, for the low Reynolds numbers appears to reach a periodic steady state after the initial transients for all of the frequency ratios that were considered, suggesting that quasi-steady models might be able to reproduce this behavior. Such models have been reported in the literature, and these models have been adapted for flapping flight based on models developed for high Reynolds number fixed wing aeroelasticity studies by including wing rotation along with translation (Ellington, 1984a, 1999), and forces due to added mass (Sane and Dickinson, 2002). In a more recent study (Wang *et al.*, 2004) the unsteady forces from experiments and with two-dimensional computations were compared with the quasi-steady model predictions. They pointed out that the force predictions, which were made by using models based on potential flow theory (Munk, 1925) for a constant pitching amplitude and constant translating speed wing, deviated substantially from the experimentally determined unsteady forces. The forces predictions from a semi-empirical model based on numerical results from steady translating wings at a fixed angle of attack were in broad qualitative agreement with the unsteady forces. However, detailed comparisons revealed that depending on the kinematics, the unsteady effects can reduce the total lift by a factor 2 to 3. In the present case, due to the wing's flexibility, the identification of the quasi-steady contributions is more complex as additional new states have been included.

Closure

In the present work, the influence of flexibility on the aerodynamic performance of a two-dimensional hovering wing section has been numerically studied. The wing model consists of two rigid links that are joined at the center with a linear torsion spring. By prescribing the kinematics of the top link, the structural system is effectively reduced to a single degree-of-freedom nonlinear oscillator. The viscous flow around this structure is described by incompressible form of Navier-Stokes equations. The combined set of equations describing the fluid and structural dynamics are integrated in time by using a scheme that can capture strongly coupled fluid-structure interactions.

The results obtained in this study demonstrate that flexibility can be beneficial in terms of enhancing the aerodynamic performance. Furthermore, it is seen that in the frequency range below the first natural frequency, the best performance is achieved when the wing is driven at a frequency close to one of the nonlinear resonances (a superharmonic resonance of order three) of the system. This behavior is seen to be common for all of the Reynolds numbers studied. In terms of the flow physics, the wake capture mechanism is enhanced partially due to a stronger flow around the wing at stroke reversal. However, it needs to be noted that the cases where the wing is driven at or close to the first natural frequency of the system were not considered in this study, and it is possible that a better aerodynamic performance may be achieved with a linear resonance and this remains to be explored.

The study also leads to the following open questions: i) why is there a performance enhancement when the system is excited at a flapping wing's nonlinear resonance and would one achieve a better performance with a nonlinear resonance compared to a linear

resonance? and ii) which kinematics is preferable from an aerodynamic efficiency standpoint? The interplay between wing flexibility and kinematics together with qualitative changes (and bifurcations) in the system dynamics as a function of the Re number require further investigation.

Acknowledgements

The authors gratefully acknowledge the support received through AFOSR Grant No. FA95500610093 and ARO Grant No. W911NF0610369. Support received from the Minta Martin Foundation is also acknowledged. They are thankful to Mr. N. Beratlis for providing the vortex circulation computing algorithm.

References

Anderson, T. J., Balachandran, B., and Nayfeh, A. H. (1994). Nonlinear resonances in a flexible cantilever beam. *J. Vibration and Acoustics* **116**, 480-484.

Bao, L., Hu, J. S., Yu, Y. L., Cheng, P., Xu, B. Q., and Tong B. G. (2006). Viscoelastic constitutive model related to deformation of insect wing under loading in flapping motion. *Appl. Math. and Mech.* **27** (6), 741-748.

Balaras, E. (2004). Modeling complex boundaries using an external force field on fixed Cartesian grids in large-eddy simulations. *Comput. Fluids* **33**, 375–404.

Berman, G. J. and Wang, Z. J. (2007). Energy-minimizing kinematics in hovering insect flight. *J. Fluid Mech.* **582**, 153-168.

Combes, S. A. and Daniel, T. L. (2003). Into thin air: contributions of aerodynamic and inertial-elastic forces to wing bending in the hawkmoth Manduca sexta. *J. Exp. Biology* **206**, 2999-3006.

Daniel, T. L. and Combes, S. A. (2002). Flexible Wings and Fins: Bending by inertial or fluid-dynamic forces? *Integr. Comp. Biol.* **42**, 1044-1049.

Dickinson, M. H., Lehmann, F. O., and Sane, S. P. (1999) Wing rotation and the aerodynamic basis of insect flight. *Science* **284**, 1954-1960.

Ellington, C. P., (1984a). The aerodynamics of hovering insect flight. Part I: The quasi-steady analysis. *Phil. Trans. R. Soc. Lond.* B **305**, 145-181.

Ellington, C. P., (1984b). The aerodynamics of hovering insect flight. Part VI: Lift and power requirements. *Phil. Trans. R. Soc. Lond.* B **305**, 145-181.

Ellington, C. P., Van den Berg, C., Willmott, A. P., and Thomas, A. L. (1996). Leading edge vortices in insect flight. *Nature* **384**, 626-630.

Ellington, C. P. (1999). The novel aerodynamics of insect flight: applications to micro-air vehicles. *J. Exp. Biology* **202**, 3439-3448.

Ennos, A. R. (1989). Inertial and aerodynamic torques on the wings of Diptera in flight. *J. Exp. Biology* **142**, 87-95.

Herbert, R. C. (2002). Modelling insect wings using the finite element method. *PhD Thesis*, University of Exeter.

Lehmann, F. O. and Dickinson, M. H. (1997). The changes in power requirements and muscle efficiency during elevated force production in the fruit fly Drosophila melanogaster. *J. Exp. Biology* **200**, 1133-1143.

Liu, H. and Kawachi, K. (1998). A numerical study of insect flight. *J. Comput. Phys.* **146**, 124-156.

Miao, J. M. and Ho, M. H. (2006). Effect of flexure on aerodynamic propulsive efficiency of flapping flexible airfoil. *J. Fluid Struct.* **22** (3), 401-419.

Miller, L. A. and Peskin, C. S. (2005). A computational fluid dynamics of 'clap and fling' in the smallest insects. *J. Exp. Biology* **208**, 195-212.

Munk, M. M. (1925). *NACA Tech. Notes* **217**, 1-6.

Nayfeh, A. H. and Balachandran, B. (1995). *Applied Nonlinear Dynamics: Analytical, Computational, and Experimental Methods*, Wiley, New York.

Ramamurti, R. and Sandberg, W. (2002). A three-dimensional computational study of the aerodynamic mechanisms of insect flight. *J. Exp. Biology* **205**, 1507-1518.

Ramamurti, R., and Sandberg, W. (2006). A computational investigation of the three-dimensional unsteady aerodynamics of Drosophila hovering and maneuvering. *J. Exp. Biology* **210**, 881-896.

Sane, S. P. and Dickinson, M. H. (2002). The aerodynamic effects of wing rotation and a revised quasi-steady model for flapping flight. *J. Exp. Biology* **205**, 1087-1096.

Song, D., Wang, H., Zeng, L., and Yin, C. (2001). Measuring the camber deformation of a dragonfly wing using projected comb fringe. *Rev. Sci. Instr.* **72** (5), 2450-2454.

Sun, M. and Tang, J. (2002). Unsteady aerodynamic force generation by a model fruit fly wing in flapping motion. *J. Exp. Biology* **205**, 55-70.

Uhlmann, M., (2005). An immersed boundary method with direct forcing for the simulation of particulate flows. J. Comput. Phys. **209** (2): 448-476.

Wang, Z. J. (2000a). Two dimensional mechanism for insect hovering. *Phys. Rev. Lett.* **85**, 2216-2219.

Wang, Z. J. (2000b). Vortex shedding and frequency selection in flapping flight. *J. Fluid Mech.* **410**: 323-341.

Wang, Z. J., Birch, J. M., and Dickinson, M. H. (2004). Unsteady forces and flows in low Reynolds number hovering flight: two-dimensional computations *vs* robotic wing experiments. *J. Exp. Biology* **207**, 449-460.

Wootton, R. J. (1999). Invertebrate paraxial locomotory appendages: design, deformation and control. *J. Exp. Biology* **202**, 3333-3345.

Wootton, R. J., Herbert, R. C., Young, P. G., and Evans, K. E. (2003). Approaches to structural modeling of insect wings. *Phil. Trans. R. Soc. Lond.* B **358**, 1577-1587.

Yang, J., and Balaras, E. (2006). An embedded-boundary formulation for large-eddy simulation of turbulent flows interacting with moving boundaries. *J. Comput. Phys.* **215** (1), 12-40.

Yang, J., Preidikman, S., and Balaras, E. (2008). A strongly-coupled, embedded-boundary method for fluid-structure Interactions of elastically mounted rigid bodies. *J. Fluids and Structures*, **24** (2), 167-182.

Figures and Tables

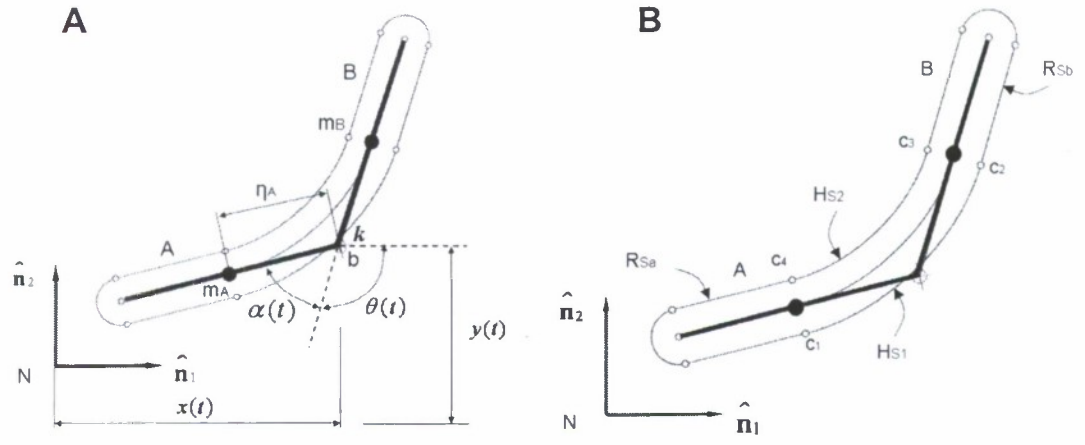

Figure 1: A) The two-link model. The rigid links A and B (thick black line) are connected at hinge *b* by a torsion spring with stiffness *k*. The variables *x(t)*, *y(t)*, *θ(t)* and *α(t)* are the generalized coordinates used to describe the wing's motion. In the hovering simulations, *x(t)*, *y(t)*, and *θ(t)* are prescribed and *α(t)* is the only degree of freedom needed to define the system. B) Decomposition of the wing's aerodynamic surfaces into rigid and deformable sections for the immersed-boundary scheme. R_{Sa} and R_{Sb} are connected at points c_1, c_2,, c_3 , and c_4 by Hermite interpolating polynomials H_{S1} and H_{S2}.

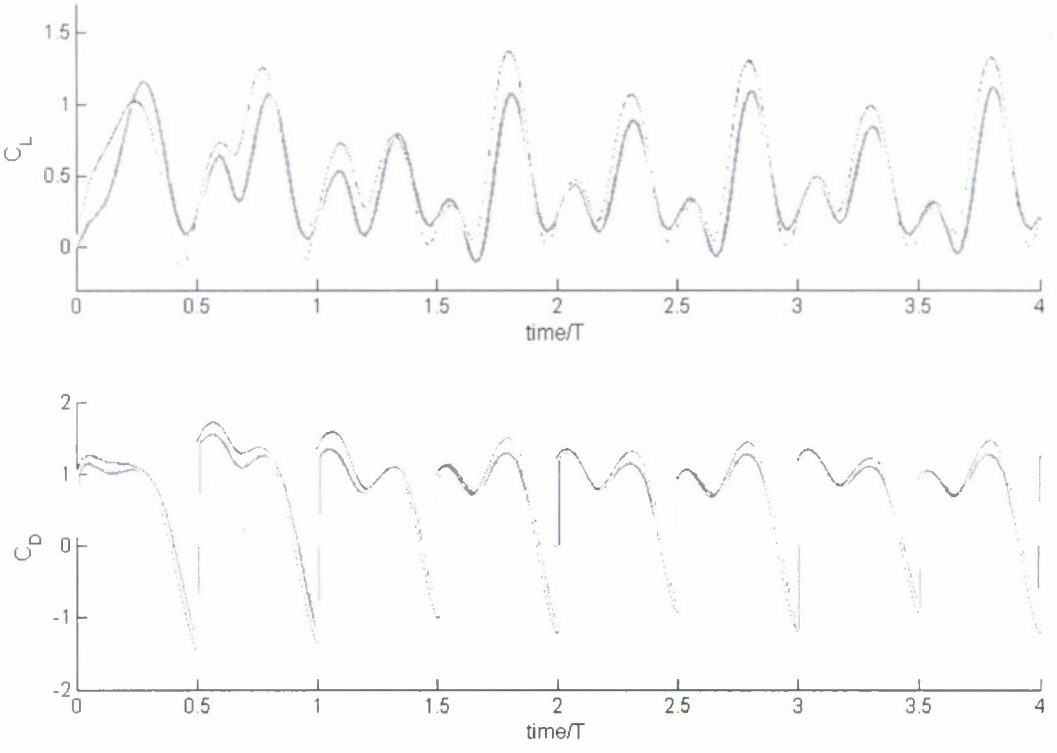

Figure 2: Time histories of lift and drag force coefficients C_D, C_L for symmetric harmonic hovering rigid link at Re = 75 and two different grid resolutions. ——— Rigid link, embedded boundary grid 1229x551; Rigid link, embedded boundary grid 666x402; and ——— Wang *et al.* (2004).

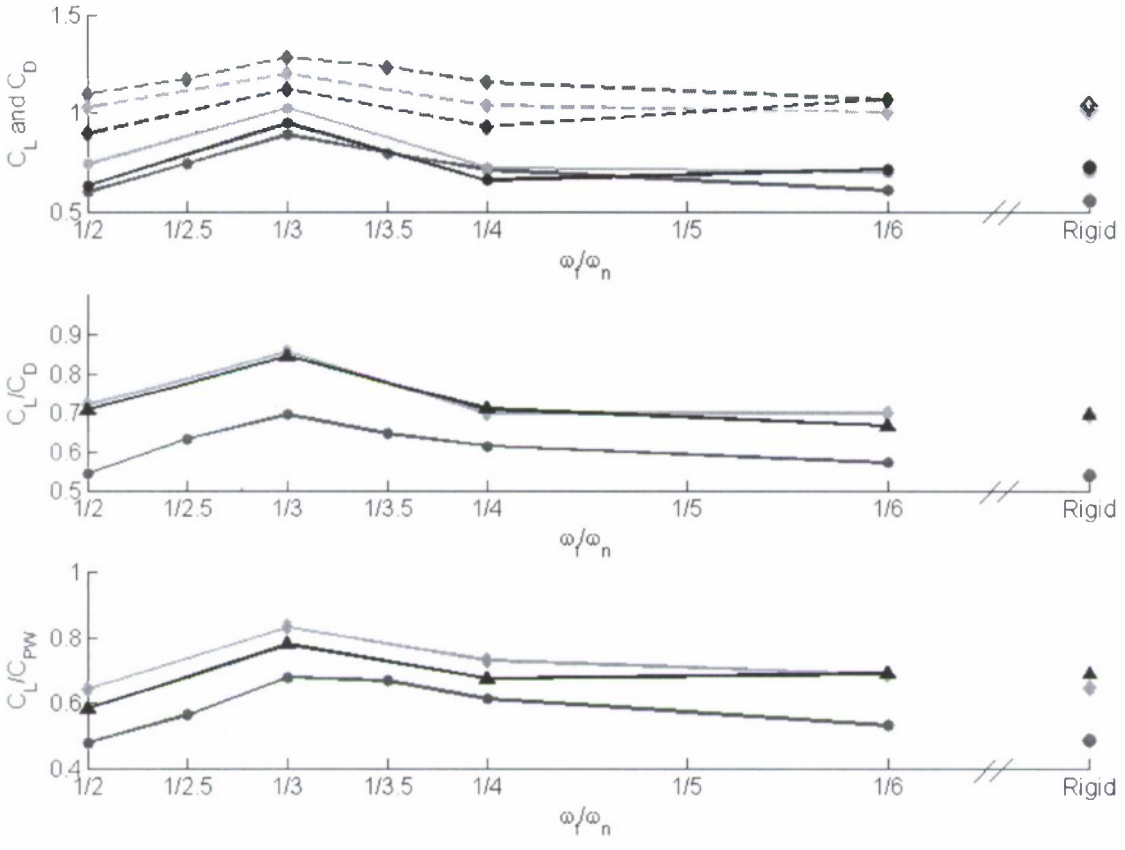

Figure 3: A) Variations of mean C_L and C_D with respect to the frequency ratio ω_f / ω_n; (—●—) for C_L at Re = 75, (—●—) for C_L at Re = 250, (—●—) for C_L at Re = 1000, (-◆-) for C_D at Re = 75, (-◆-) for C_D at Re = 250, and (-◆-) for C_D at Re = 1000. B) Ratio of mean C_L/C_D versus ω_f / ω_n; (—●—) for Re = 75, (—◆—) for Re = 250, and (—▲—) for Re = 1000. C) Mean lift coefficient per unit of driving power coefficient versus ω_f / ω_n; same definitions as in B. The results obtained for the rigid wing are also plotted for comparison.

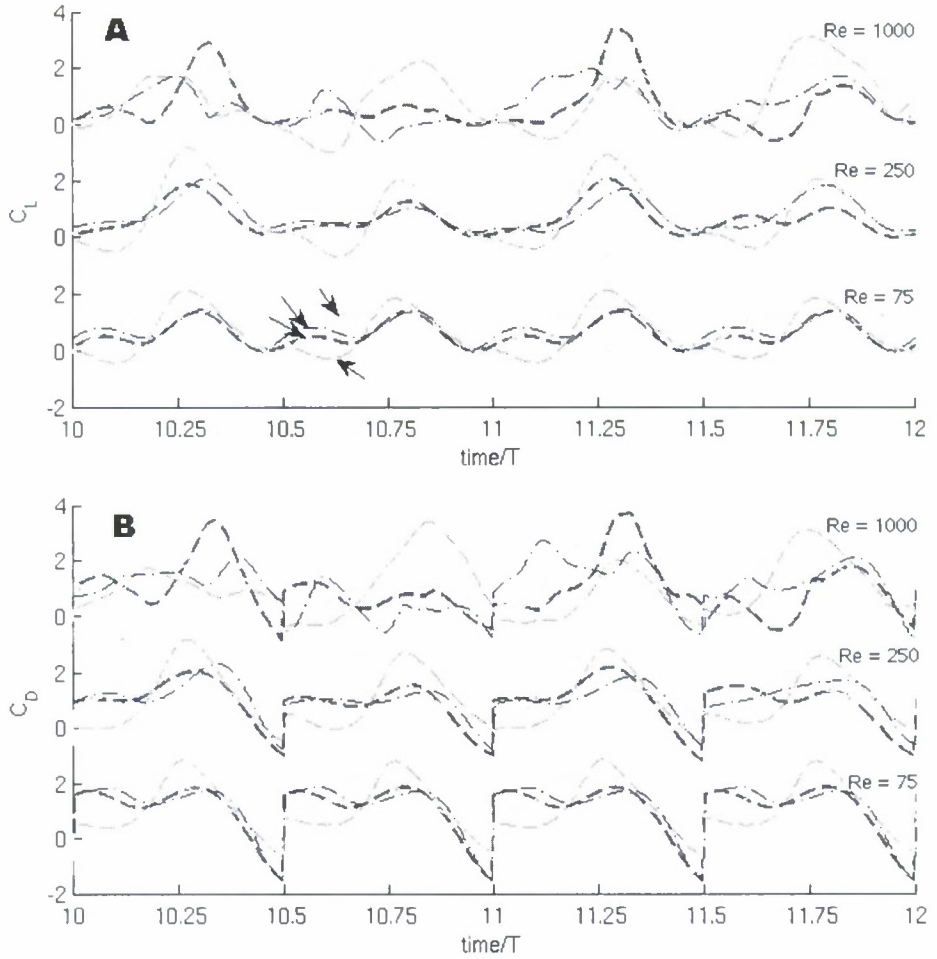

Figure 4: Time histories of lift and drag coefficients for Re = 75, 250 and 1000: A) lift coefficient and B) drag coefficient; — — rigid wing; – – – flexible wing with $\omega_f / \omega_n = 1/2$; ——— flexible wing with $\omega_f / \omega_n = 1/3$; -·-·- flexible wing with $\omega_f / \omega_n = 1/4$.

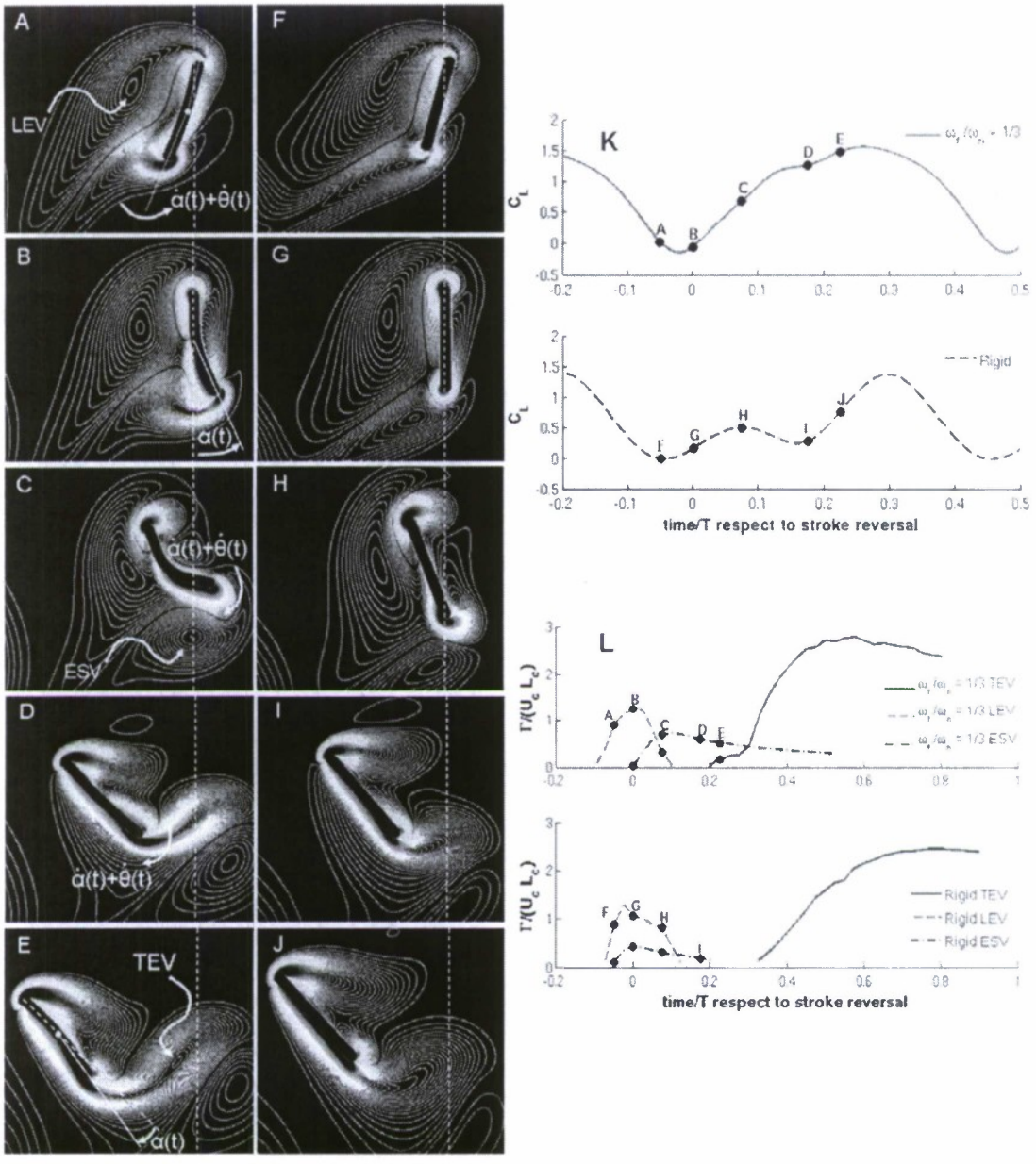

Figure 5: Comparison of the rigid wing's performance during stroke reversal with respect to that of the flexible wing at a frequency ratio of $\omega_f / \omega_n = 1/3$ at Re = 75. A, B, C, D, and E: Vorticity contours for flexible wing with $\omega_f / \omega_n = 1/3$ at five time instances: t/T = -0.0491, 0.0009, 0.0759, 0.1760, and 0.2260 ($\omega_{\min} = -10$, $\omega_{\max} = 10$, and 80 contours). F, G, H, I, and J: Vorticity contours for the rigid wing at the same time locations. The white dashed lines indicate the end of stroke position; (K) lift coefficient history; and (L) histories of circulation of LEV, ESV, and TEV vortices.

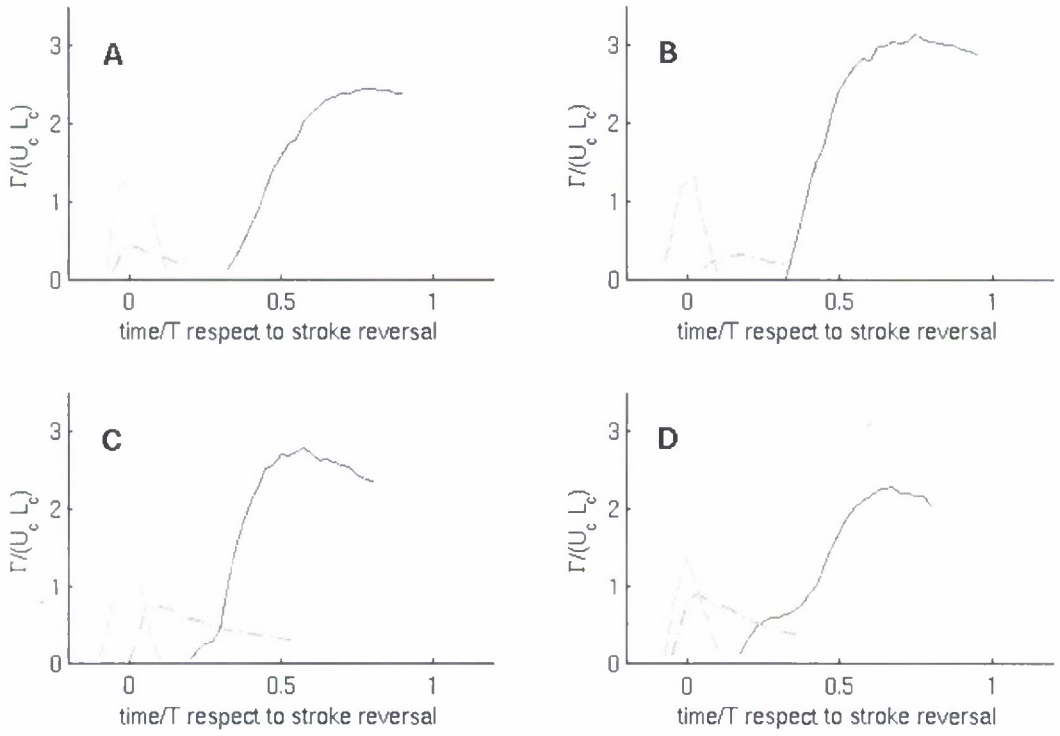

Figure 6: Averaged circulations as a function of time at Re = 75; —— TEV; - - - - LEV; - · - · - ESV. A) Rigid wing, B) flexible wing with $\omega_f / \omega_n = 1/2$, and C) flexible wing with $\omega_f / \omega_n = 1/3$, and D) flexible wing with $\omega_f / \omega_n = 1/4$.

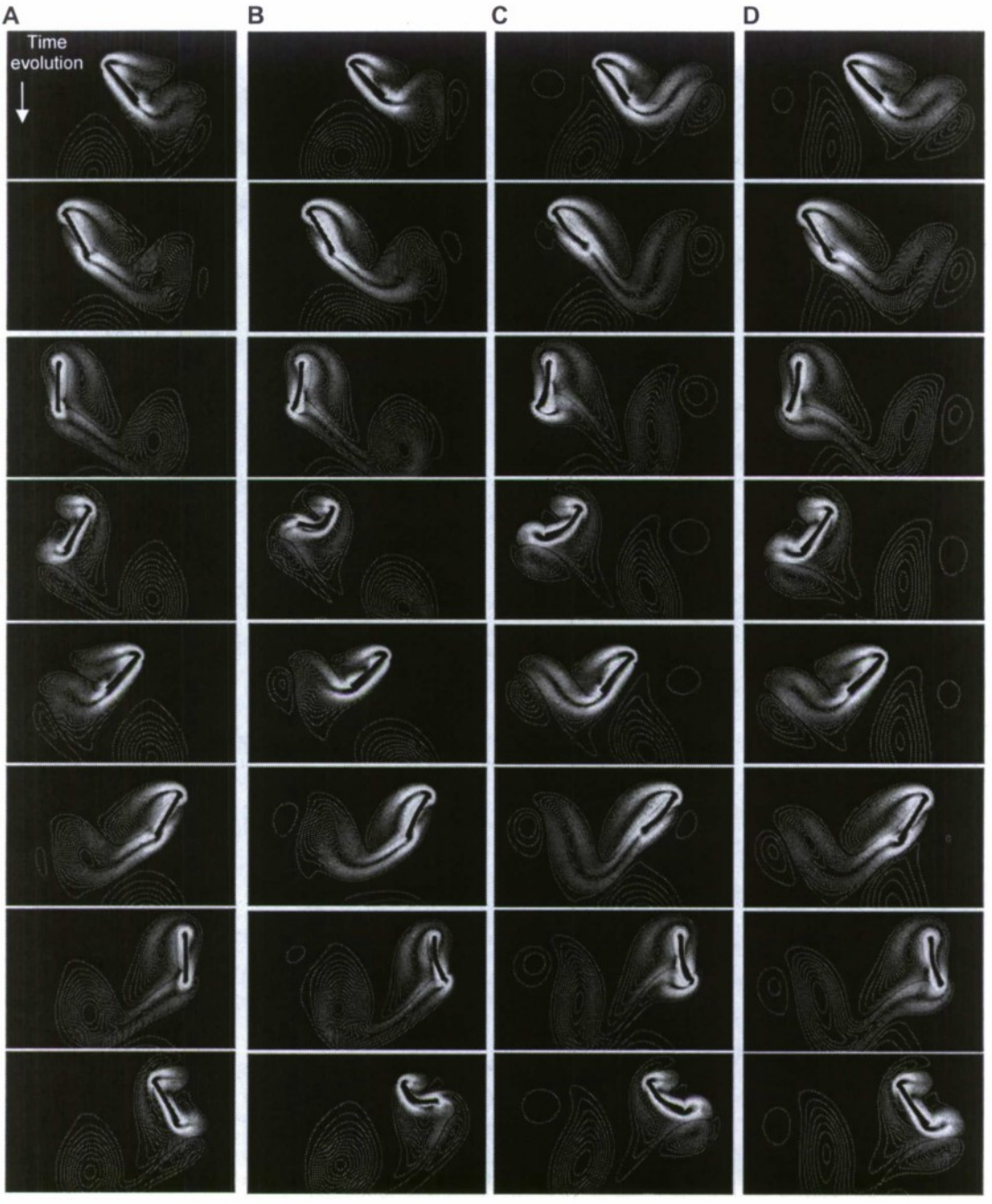

Figure 7: Instantaneous vorticity contours at Re = 75. Contours range from -10 (blue) to 10 (red) with 80 intervals. Column A: rigid wing; Columns B, C, and D: flexible wings with $\omega_f / \omega_n = 1/2,\ 1/3,$ and $1/4$, respectively.

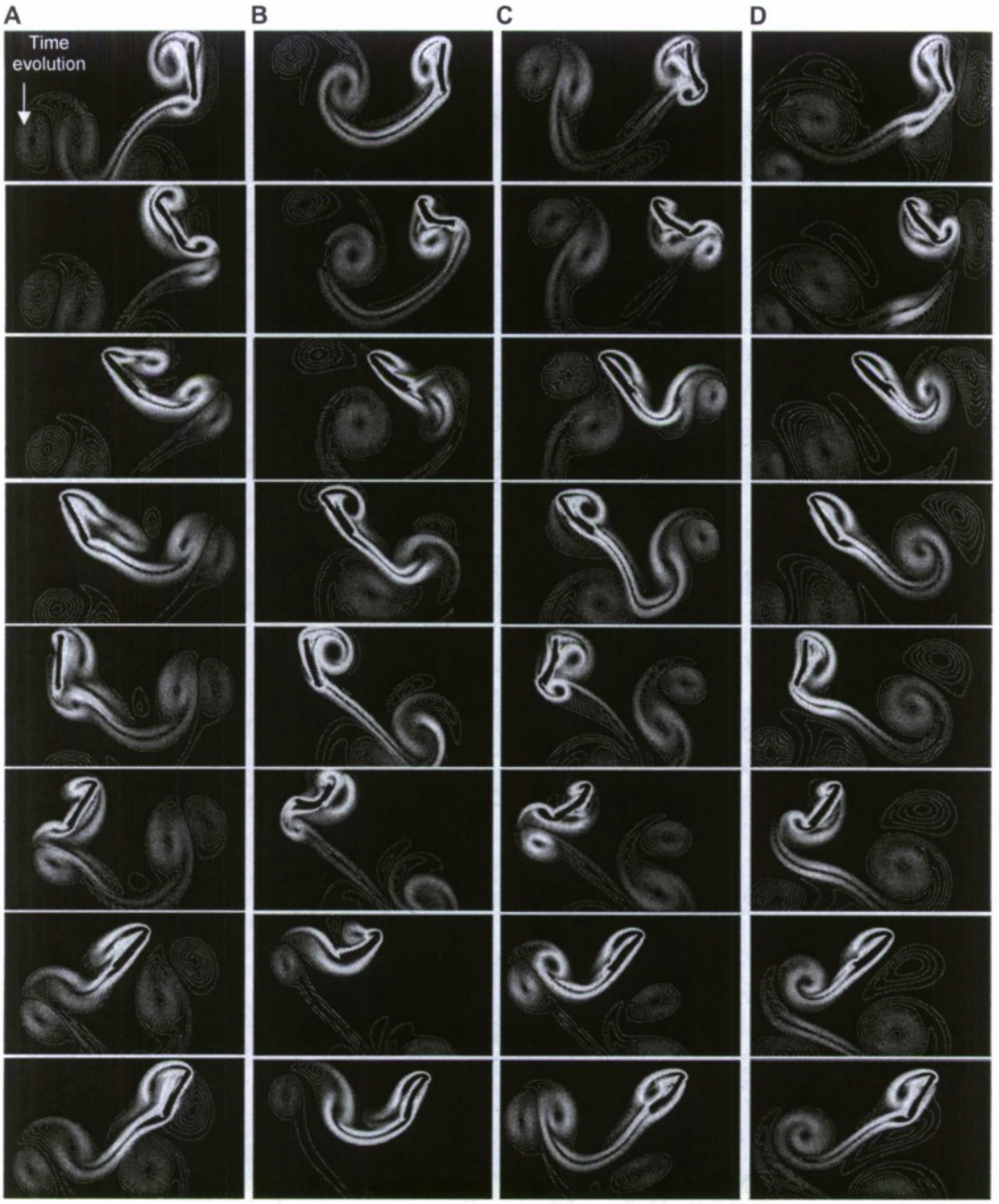

Figure 8: Instantaneous vorticity contours at Re = 250. Contours range from -10 (blue) to 10 (red) with 80 intervals. Column A: rigid wings; Columns B, C, and D: flexible wings with $\omega_f / \omega_n = 1/2,\ 1/3,$ and $1/4$, respectively.

Degree of flexibility	Circulation TEV	Time TEV	Circulation LEV	Time LEV	Circulation ESV	Time ESV
Rigid	2.44	0.78	1.30	-0.02	0.44	0.001
$\omega_f / \omega_n = 1/2$	3.14	0.75	1.30	0.03	0.31	0.18
$\omega_f / \omega_n = 1/3$	2.78	0.58	1.25	0.001	0.72	0.10
$\omega_f / \omega_n = 1/4$	2.29	0.68	1.36	0.001	0.87	0.03
$\omega_f / \omega_n = 1/6$	2.36	0.80	1.43	0.001	0.59	0.02

Table 1: Values of maximum mean circulation obtained for the TEV, LEV, and ESV at Re=75. Time is defined in the same way as in Figure 6.